A Study of Ocean-Like Surface Thermal Emission and Reflection Using Voronovich's Small Slope Approximation

Joel T. Johnson
Dept. of Electrical and Computer Engineering and ElectroScience Laboratory
The Ohio State University
Columbus, OH 43210
Email: johnson@ece.osu.edu

***Abstract*— Monte Carlo simulations are used to compute average direct surface thermal emission and reflected atmospheric radiation using the "active" small slope approximation of Voronovich. The surfaces considered are realizations of an ocean-like spectrum, and contain features ranging from 64 to 0.5 electromagnetic wavelengths. The parallel computing approach of the study is described, and results are compared with predictions from the commonly applied "two-scale" theory of sea emission. Results show a reasonable level of agreement in a small height surface case, which degrades as the surface height is increased.**

I. Introduction

Interest in the computation of microwave polarimetric thermal emission from the sea surface has recently increased due to the greater availability of satellite data from the WindSAT mission [1]. Accurate and efficient "forward models" of sea emission are required in order to perform "physically based" retrievals of sea surface wind vector through an optimization process. A theory of sea emission can be developed based on existing theories of scattering from the sea surface in combination with Kirchhoff's law of thermal emission. The "two-scale" theory of scattering from the sea surface extended in [2] to compute polarimetric sea brightnesses has become the most commonly applied method. The "passive" small-slope approximation (SSA) [3]-[5] is an alternate approach based on use of the small perturbation method (SPM) for computing surface scattering coefficients. Although the SPM is a series in surface height for scattering coefficients, a fortuitous cancellation occurs when computing emission that results in a small slope theory of surface brightness temperatures [3].

A final theory of scattering from the sea surface is the "active" small-slope approximation of Voronovich [6]. The active SSA expresses surface scattering cross sections as a series in surface "quasi-slope"; at present, two terms in the scattered field series are known for three dimensional scattering problems with penetrable surfaces. When both terms in the SSA series are included, it has been shown that the active SSA reproduces the basic form of the active two-scale model in appropriate limits, without requiring choice of a "cutoff" wavenumber to divide long and short surface length scales as in the two-scale theory [7]. The active SSA is attractive for this reason, but computation of the second series term is extremely expensive compared to the two-scale model. For this reason, no previous studies have reported on use of the active SSA for computing sea surface emission through Kirchhoff's Law.

Because all of these models are approximate theories of sea emission, establishing the accuracy of each is difficult. Although comparison with numerically exact theories of sea emission [8]-[9] could be applied for such an assessment, such methods have limited accuracy as well due to computational issues and have exponentially larger computational requirements. An incomplete assessment can be obtained through intercomparison of approximate theories so that the level of agreement can be observed. Note that results from all of these models are dependent on the forms used for the sea surface spectrum as well as the sea water permittivity.

In this paper, the active SSA is applied to compute direct sea surface emission and reflected atmospheric emission. The formulation of the method is described in the next section, and the numerical procedure developed for this computation is discussed in Section III. Section IV presents results and comparisons with predictions of the two-scale and passive SSA models.

II. Active SSA Formulation

The computation of surface brightness temperatures through Kirchhoff's Law requires an integration over surface bistatic scattering cross sections. When two terms in the SSA field series are used, the resulting bistatic cross sections contain three terms, involving the power in each SSA term and the correlation between fields in the two terms. These expressions can be analytically averaged to obtain results in terms of a two-dimensional integration over space that contains the surface correlation function [10]. The second and third terms in the series also include inner integrations over the surface spectrum [10]. When these cross section expressions are applied in Kirchhoff's Law, the final result for surface brightness temperatures is a 6- or 8-fold integration depending on whether two or three series terms are retained. Although such scattering coefficient expressions have been evaluated for surfaces with a Gaussian correlation function [10], use of a multi-scale sea surface model further complicates the computations.

Due to this complexity, an alternate approach was pursued based on a Monte Carlo simulation of the SSA using periodic

surfaces, as in [11]. Because fields, rather than powers, are computed in this approach, the scattering coefficient integrations required are only 4 dimensional for a single surface realization. Furthermore, a highly efficient algorithm can be developed based on use of the fast-Fourier-transform (FFT), as will be described later. While repeated computations over multiple realizations are required, averages will be shown to converge to an acceptable accuracy with a moderate number of surface realizations. The use of periodic surfaces also results in a discretized scattered field (i.e. the "Floquet modes"), so that the Kirchhoff's Law integration over scattered angles becomes discretized.

Use of a Monte Carlo simulation with deterministic surfaces, however, limits the range of surface scales that can be considered, as surface profiles must be discretized into a finite set of points. Because resolution of the "Bragg" portion of the sea spectrum is important for brightness computations, the surface must be sampled on a sub-wavelength scale, and the range of "large-scale" surface features that can be resolved becomes limited by computational requirements. The discretization of scattered fields is also an issue, although when surface periods large compared to wavelength are used, the discretization becomes sufficiently fine to approximate scattering from a continuous surface.

A. Basic formulation

Consider a deterministic periodic surface profile, $z = f(x,y)$, with periods P_x and P_y in the x and y directions respectively, which separates free space (permittivity ϵ_0, permeability μ_0) for $z > f(x,y)$ from a homogeneous non-magnetic dielectric medium with permittivity $\epsilon_d = \epsilon\epsilon_0$ for $z < f(x,y)$. This periodic surface can also be expressed in terms of its Fourier series coefficients,

$$f(x,y) = \sum_{n=-\infty}^{\infty}\sum_{m-\infty}^{\infty} \exp\left(i\frac{2\pi nx}{P_x}\right)\exp\left(i\frac{2\pi my}{P_y}\right)h_{n,m} \quad (1)$$

$$h_{n,m} = \frac{1}{P_x}\frac{1}{P_y}\int_0^{P_x}dx\int_0^{P_y}dy \exp\left(-i\frac{2\pi nx}{P_x}\right)\exp\left(-i\frac{2\pi my}{P_y}\right)f(x,y). \quad (2)$$

Henceforth it will be assumed that all sums are from $-\infty$ to ∞ unless otherwise notated.

Consider an incident electromagnetic plane wave which illuminates this periodic surface from the free space region, with an electric field given by

$$\mathbf{E}^i = \hat{e}_i \exp\left(i\mathbf{k}_i\cdot\mathbf{r}\right) \quad (3)$$

where $\hat{e}_i$ represents the polarization vector of the incident electric field,

$$\mathbf{k}_i = k_0\hat{k}_i = \hat{x}k_{xi} + \hat{y}k_{yi} - \hat{z}k_{zi} \quad (4)$$

represents the propagation vector of the incident plane wave with wavenumber $k_0 = 2\pi/\lambda$, and

$$\mathbf{r} = \hat{x}x + \hat{y}y + \hat{z}z \quad (5)$$

is a position vector in Cartesian space. Note an $\exp(-i\omega t)$ time convention is assumed.

Under the Rayleigh hypothesis, the scattered field consists of a sum of up-going plane waves (or "Floquet modes") which can be written as

$$\mathbf{E}^s = \sum_m\sum_n\left[\hat{h}_s^{n,m}\alpha_{n,m} + \hat{v}_s^{n,m}\beta_{n,m}\right]\exp\left(i\mathbf{k}_s^{n,m}\cdot\mathbf{r}\right) \quad (6)$$

Here α and β are the unknown complex amplitudes of the scattered Floquet modes in horizontal and vertical polarizations, respectively. Scattered plane wave propagation vectors are defined by the Floquet theorem as

$$\mathbf{k}_s^{n,m} = \hat{x}k_{xn} + \hat{y}k_{ym} + \hat{z}k_{znm} \quad (7)$$

where

$$k_{xn} = k_{xi} + \frac{2\pi n}{P_x} \quad (8)$$

$$k_{ym} = k_{yi} + \frac{2\pi m}{P_y} \quad (9)$$

$$k_{\rho nm} = \sqrt{k_{xn}^2 + k_{ym}^2} \quad (10)$$

$$k_{znm} = \sqrt{k_0^2 - k_{\rho nm}^2} \quad (11)$$

$$k_{z1nm} = \sqrt{k_0^2\epsilon - k_{\rho nm}^2} \quad (12)$$

Modes for which $k_{\rho nm}$ becomes greater than k_0 or k_1 have k_{znm} and k_{z1nm} respectively defined so that attenuation occurs as fields propagate away from the surface boundary. The definition of k_{z1nm} above involves the vertical component of the propagation vector below the interface, and is required in evaluating the SPM kernels described below. Because only propagating Floquet modes contribute to the surface brightness, and because scattered modes above the surface become evanescent when $k_{\rho nm} > k_0$, it is clear in the above equations that a larger number of propagating scattered modes ((n,m) pairs) is obtained as the surface periods become larger.

Orthogonal horizontal and vertical polarization vectors for the incident and scattered fields are defined as

$$\hat{h}_i = \hat{x}\frac{k_{yi}}{k_{\rho i}} - \hat{y}\frac{k_{xi}}{k_{\rho i}} \quad (13)$$

$$\hat{h}_s^{n,m} = \hat{x}\frac{k_{ym}}{k_{\rho nm}} - \hat{y}\frac{k_{xn}}{k_{\rho nm}} \quad (14)$$

$$\hat{v}_i = \hat{x}\frac{k_{xi}k_{zi}}{k_0k_{\rho i}} + \hat{y}\frac{k_{yi}k_{zi}}{k_0k_{\rho i}} + \hat{z}\frac{k_{\rho i}}{k_0} \quad (15)$$

$$\hat{v}_s^{n,m} = -\hat{x}\frac{k_{xn}k_{znm}}{k_0k_{\rho nm}} - \hat{y}\frac{k_{ym}k_{znm}}{k_0k_{\rho nm}} + \hat{z}\frac{k_{\rho nm}}{k_0} \quad (16)$$

B. SSA fields

The SSA field series for Floquet mode complex amplitudes $\gamma_{n,m} = \alpha_{n,m}$ or $\beta_{n,m}$ has the form $\gamma_{n,m} = \gamma_{n,m}^{(1)} + \gamma_{n,m}^{(2)} + \cdots$,

with

$$\gamma^{(1)}_{n,m} = \frac{i\ g^{(1)}_{\rm spm}}{k_{dz}\ P_x\ P_y}\int_0^{P_x} dx \int_0^{P_y} dy\ e^{-i\mathbf{k}_d\cdot\mathbf{r}} \tag{17}$$

$$\gamma^{(2)}_{n,m} = \frac{i}{2\ k_{dz}\ P_x\ P_y}\int_0^{P_x} dx \int_0^{P_y} dy\ e^{-i\mathbf{k}_d\cdot\mathbf{r}} \sum_{n'}\sum_{m'} e^{i\left(k_{xn'}x+k_{ym'}y\right)} h_{n',m'}\, g_{\rm ssa}\left(k_{xn'},k_{ym'}\right) \tag{18}$$

as the first two series terms. Here

$$\mathbf{k}_d = \hat{x}k_{dx}+\hat{y}k_{dy}+\hat{z}k_{dz} \tag{19}$$

$$= \hat{x}\left(k_{xn}-k_{xi}\right)+\hat{y}\left(k_{ym}-k_{xi}\right)+\hat{z}\left(k_{znm}+k_{zi}\right) \tag{20}$$

and $z=f(x,y)$ is used in the integration. The term $g^{(1)}_{\rm spm}$ is the first order polarization coefficient from the SPM solution, as defined in [12], and is applied for the appropriate polarization when computing $\gamma^{(1)}_{n,m}$. The term $g_{\rm ssa}$ is the SSA kernel function, and is defined as

$$g_{\rm ssa}(k_{xn'},k_{ym'}) = g^{(2)}_{\rm spm}(k_{xi}+k_{xn'},k_{yi}+k_{ym'}) + g^{(2)}_{\rm spm}(k_{xn}-k_{xn'},k_{ym}-k_{ym'}) + ik_{dz}g^{(1)}_{\rm spm} \tag{21}$$

where $g^{(2)}_{\rm spm}$ is the second order polarization coefficient from the SPM solution, as defined in [12], and again is applied for the appropriate polarization when computing $\gamma^{(2)}_{n,m}$. Finally, the primed wave number quantities are defined as

$$k_{xn'} = \frac{2\pi n'}{P_x} \tag{22}$$

$$k_{ym'} = \frac{2\pi m'}{P_y} \tag{23}$$

The above formulation applies for both horizontally and vertically polarized incident fields. However, in computing polarimetric brightness temperatures, γ values for horizontal and vertical incidence must be considered simultaneously. For this reason, it is convenient to introduce a new notation for Floquet mode complex amplitudes as follows, with $s=1$ and 2,

$$f^{hh,(s)}_{n,m} = \alpha^{(s)}_{n,m} \tag{24}$$

$$f^{vh,(s)}_{n,m} = \beta^{(s)}_{n,m} \tag{25}$$

with a horizontally polarized incident field, and

$$f^{hv,(s)}_{n,m} = \alpha^{(s)}_{n,m} \tag{26}$$

$$f^{vv,(s)}_{n,m} = \beta^{(s)}_{n,m} \tag{27}$$

with a vertically polarized incident field.

C. Power formulation

Following [12], the fraction of incident power reflected into one polarization of a single Floquet mode can be expressed as

$$\mathrm{Re}\left\{\frac{k_{znm}}{k_{zi}}\right\}\left|f^{qr}_{n,m}\right|^2, \tag{28}$$

where qr refers to the polarization superscript. The "Real" operator on the left hand side serves to exclude evanescent modes, and will be neglected in what follows assuming that only propagating modes are considered. Given the SSA series solution for $f_{n,m}$, the corresponding fractional power is

$$\frac{k_{znm}}{k_{zi}}\left|f^{qr}_{n,m}\right|^2 = \frac{k_{znm}}{k_{zi}}\left|f^{qr,(1)}_{n,m}+f^{qr,(2)}_{n,m}+f^{qr,(3)}_{n,m}+\cdots\right|^2 \tag{29}$$

Collecting terms of identical order yields

$$\frac{k_{znm}}{k_{zi}}\left|f^{qr}_{n,m}\right|^2 = \frac{k_{znm}}{k_{zi}}\left\{\left(\left|f^{qr,(1)}_{n,m}\right|^2\right)+\left(2\mathrm{Re}\left\{f^{qr,(1)*}_{n,m}f^{qr,(2)}_{n,m}\right\}\right)+\left(\left|f^{qr,(2)}_{n,m}\right|^2+2\mathrm{Re}\left\{f^{qr,(1)*}_{n,m}f^{qr,(3)}_{n,m}\right\}\right)+\cdots\right\} \tag{30}$$

The total power reflected in a particular polarization can be obtained by summing the above over all propagating scattered modes. Separating this into three terms yields

$$P_2 = \sum_n\sum_m \frac{k_{znm}}{k_{zi}}\left|f^{qr,(1)}_{n,m}\right|^2 \tag{31}$$

$$P_3 = \sum_n\sum_m \frac{k_{znm}}{k_{zi}}\,2\mathrm{Re}\left\{f^{qr,(1)*}_{n,m}f^{qr,(2)}_{n,m}\right\} \tag{32}$$

$$P_4 = \sum_n\sum_m \frac{k_{znm}}{k_{zi}}\left(\left|f^{qr,(2)}_{n,m}\right|^2+2\mathrm{Re}\left\{f^{qr,(1)*}_{n,m}f^{qr,(3)}_{n,m}\right\}\right) \tag{33}$$

From the above, it is clear that there are three contributions to the scattered fractional power that result from the first and second SSA field series terms. The first term will be labeled as "SSA2" in what follows (since it is a first order term squared), while the sum of the first and second terms (P_2+P_3) will be labeled "SSA3", and the sum of all three terms ($P_2+P_3+P_4$) "SSA4". Note that the final term properly includes contributions from both the second and third SSA field series terms; however the third SSA field series term is not known at present for penetrable surfaces, and is therefore not considered in this study. Due to this limitation, comparisons of SSA4 and SSA3 power results can provide only incomplete information on convergence of the SSA series.

D. Brightness temperatures

Applying Kirchhoff's Law for the computation of polarimetric brightness temperatures [2],[13], and using a procedure similar to that of the previous section yields:

$$T^{(2)}_h = T_s - T_s\sum_n\sum_m \frac{k_{znm}}{k_{zi}}\left(\left|f^{hh,(1)}_{n,m}\right|^2+\left|f^{vh,(1)}_{n,m}\right|^2\right) \tag{34}$$

$$T^{(2)}_v = T_s - T_s\sum_n\sum_m \frac{k_{znm}}{k_{zi}}\left(\left|f^{hv,(1)}_{n,m}\right|^2+\left|f^{vv,(1)}_{n,m}\right|^2\right) \tag{35}$$

$$U^{(2)} = T_s \sum_n \sum_m \frac{k_{znm}}{k_{zi}} 2\mathrm{Re}\left\{ f_{n,m}^{hv,(1)} f_{n,m}^{hh,(1)*} + f_{n,m}^{vv,(1)} f_{n,m}^{vh,(1)*} \right\} \quad (36)$$

$$V^{(2)} = T_s \sum_n \sum_m \frac{k_{znm}}{k_{zi}} 2\mathrm{Im}\left\{ f_{n,m}^{hv,(1)} f_{n,m}^{hh,(1)*} + f_{n,m}^{vv,(1)} f_{n,m}^{vh,(1)*} \right\} \quad (37)$$

at second order, with

$$T_h^{(3)} = -T_s \sum_n \sum_m \frac{k_{znm}}{k_{zi}} 2\mathrm{Re}\left\{ f_{n,m}^{hh,(1)} f_{n,m}^{hh,(2)*} + f_{n,m}^{vh,(1)} f_{n,m}^{vh,(2)*} \right\} \quad (38)$$

$$T_v^{(3)} = -T_s \sum_n \sum_m \frac{k_{znm}}{k_{zi}} 2\mathrm{Re}\left\{ f_{n,m}^{hv,(1)} f_{n,m}^{hv,(2)*} + f_{n,m}^{vv,(1)} f_{n,m}^{vv,(2)*} \right\} \quad (39)$$

$$U^{(3)} = T_s \sum_n \sum_m \frac{k_{znm}}{k_{zi}} 2\mathrm{Re}\left\{ f_{n,m}^{hv,(2)} f_{n,m}^{hh,(1)*} + f_{n,m}^{hv,(1)} f_{n,m}^{hh,(2)*} + f_{n,m}^{vv,(2)} f_{n,m}^{vh,(1)*} + f_{n,m}^{vv,(1)} f_{n,m}^{vh,(2)*} \right\} \quad (40)$$

$$V^{(3)} = T_s \sum_n \sum_m \frac{k_{znm}}{k_{zi}} 2\mathrm{Im}\left\{ f_{n,m}^{hv,(2)} f_{n,m}^{hh,(1)*} + f_{n,m}^{hv,(1)} f_{n,m}^{hh,(2)*} + f_{n,m}^{vv,(2)} f_{n,m}^{vh,(1)*} + f_{n,m}^{vv,(1)} f_{n,m}^{vh,(2)*} \right\} \quad (41)$$

at third order, and fourth order results identical to those of equations (34) to (37) except that $f_{n,m}^{qr,(2)}$ quantities are used in place of $f_{n,m}^{qr,(1)}$, and the constant T_s term is neglected in the linear channels. Here T_h and T_v refer to brightness temperatures in the horizontally and vertically polarized channels, respectively, while U and V refer to the real and imaginary parts of the correlations between horizontal and vertical received fields, respectively. The U and V brightnesses will also be referred to as the third and fourth Stokes brightnesses in what follows. T_s indicates the physical temperature of the sea surface, assumed to be 285 K throughout the remainder of this study. The terms "SSA2", "SSA3", and "SSA4" again will be used to refer to partial sums of the three brightness terms.

Typical models of the sea surface spectrum include only constant and second azimuthal harmonic variations in azimuth. It has been shown [4] that the resulting brightness temperatures are of the form

$$\begin{bmatrix} T_h \\ T_v \\ U \\ V \end{bmatrix} \approx \begin{bmatrix} T_{h0} + T_{h2} \cos 2\phi_i \\ T_{v0} + T_{v2} \cos 2\phi_i \\ U_2 \sin 2\phi_i \\ V_2 \sin 2\phi_i \end{bmatrix} \quad (42)$$

where ϕ_i denotes the azimuth angle between the radiometer look direction and wind direction. Although a first azimuthal harmonic variation is also observed in experimental data, simple Gaussian random process models of the sea surface cannot capture the associated up/down wind asymmetries of the surface. Because a Gaussian random process model of the sea surface is used in this study, only the zeroth (i.e. T_{h0} and T_{v0}) and second (i.e. T_{h2}, T_{v2}, U_2, and V_2) azimuthal harmonics are of interest. The second azimuthal harmonics typically capture brightness variations due to any up/cross wind asymmetries of the surface.

E. Reflected atmospheric power

In addition to the computation of direct surface emission, prediction of reflection of the downwelling atmospheric brightness is also of interest [14]-[15]. Because downwelling atmospheric brightness is incident upon the surface from the entire upper hemisphere, the observed reflected atmospheric brightness is obtained by integrating over angle the downwelling brightness times surface bistatic scattering coefficients so that reflection into the radiometer observation direction is achieved. The resulting expressions are very similar to those of equations (34)-(41), with a few modifications. In particular, the constant T_s terms in the $T_h^{(2)}$ and $T_v^{(2)}$ equations are removed, the factor T_s multiplying all sums over n and m is replaced by -1, and the factor k_{znm}/k_{zi} inside all sums is replaced by $(k_{znm}/k_{zi})T_{atm}(\theta)$. Here $T_{atm}(\theta)$ refers to the downwelling atmospheric brightness at zenith angle

$$\theta = \cos^{-1}(k_{znm}/k_0) \quad (43)$$

In the results of Section IV, a simple one-layer model of downwelling atmospheric brightness is used:

$$T_{atm}(\theta) = T_A \left(1 - \exp\left[-\tau \sec\theta\right]\right) \quad (44)$$

Here T_A is set to 285 K, and τ represents the zenith opacity of the atmosphere in Nepers. Results will be shown for τ values ranging from 0.01 to 0.5; specular atmospheric brightnesses (i.e. $T_{atm}(\theta_i)$) then range from 4.9 to 165.8 K with $\theta_i = 55°$.

A simple approximation of reflected downwelling atmospheric effects can be developed by modeling the downwelling brightness as independent of angle

$$T_{atm}(\theta) \approx T_{atm}(\theta_i) \quad (45)$$

In this case, the reflected atmosphere equations become very similar to the direct surface emission equations, with the exception that T_s is replaced by $-T_{atm}(\theta_i)$ and the constant T_s terms in the linear channels are omitted. Because surface emitted second azimuthal harmonics are not affected by the constant T_s term in the linear channels, the simple approximation indicates that reflected atmospheric brightness should produce second azimuthal harmonics of opposite sign to those in direct surface emission. Results in Section IV will examine the accuracy of this prediction when the more complete model of the downwelling atmospheric brightness of equation (44) is used.

III. Computational issues

Computation of the active SSA brightness for a single surface realization requires evaluation of equations (17) and (18) to determine the polarimetric Floquet mode amplitudes $f_{n,m}^{qr,(s)}$

for the four polarimetric quantities of equations (24)-(27), for $s = 1$ and 2, and for all propagating Floquet modes n, m. Once these quantities are known, equations (34)-(41) are used to find the brightnesses, and the modified versions described in the previous section are used to determine reflected atmospheric brightnesses. The entire process is repeated for the multiple realizations in the Monte Carlo simulation. When surface periods large compared to the electromagnetic wavelength are used (as is desirable for simulating multi-scale sea surfaces), the number of propagating Floquet modes can become large, making efficient computations necessary.

When the integrations over the surface profile are discretized, equations (17) and (18) require computation of 2 and 4-fold sums, respectively; an examination of the inner sum in equation (18) shows it to have the form of a Fourier transform, so that the fast-Fourier-transform (FFT) algorithm can be used for efficient computations. This FFT operation involves the SSA kernel function for a particular mode n, m and the surface Fourier coefficients. Because evaluation of the SSA kernel function itself requires substantial CPU time, it is highly desirable to store this function in memory as multiple surface realizations are considered. An algorithm with an outer loop over Floquet modes and an inner loop over surface realizations is thus more efficient; surface realizations can be re-generated as needed by restoring an initial seed value to the random number generator used in surface generation.

Even when these methods are used, the large number of Floquet modes involved still makes computations problematic for a single processor when large surface periods are considered. A parallel implementation of the algorithm was developed to overcome these limitations. In this algorithm, the set of Floquet modes is divided among 16 processors; again the surfaces considered by each processor are identical through control of the random number generator seed value. To capture brightness variations with azimuthal angle, computations were performed for azimuth observation angles of 0, 30, 60, and 90 degrees; the results were then used to extract the zeroth and second azimuthal harmonic terms when necessary. The final parallel simulation used 64 processors, composed of groups of 16 processors used for each of the four azimuthal angles considered.

To facilitate atmospheric reflection computations for multiple τ values, the parallel algorithm was developed to output the polarimetric amplitudes $f_{n,m}^{qr,(s)}$ for each surface realization; although the resulting files are large, reflected atmospheric brightnesses can be obtained for multiple τ values in a post-processing evaluation of equations (34)-(41). The stored set of $f_{n,m}^{qr,(s)}$ values can be applied in other studies of bistatic scattering from rough surfaces as well.

A. Specific cases considered

The results considered here used surfaces of 64λ by 64λ, where λ is the electromagnetic wavelength, sampled into 256 by 256 points. This surface size was selected as a compromise between the computational resources available and the desire to simulate as large an ocean-like surface as possible. Surface length scales shorter than $\lambda/2$ were also removed in the simulation, in order to avoid aliasing issues in the SSA computation. When considering true sea surfaces, 64λ at microwave frequencies captures only a small portion of the "long-wave" region; however this portion should be sufficient to produce some of the long-wave "tilting" effects predicted by the two-scale model, so that the basis of this two-scale approximation can be investigated. Simulations were also performed for a second set of 64λ by 64λ surfaces, in which surface length scales larger than 4λ were additionally removed. In this case, large scale "tilting" effects should be minimized, and total surface height will be small compared to the wavelength. This set of surfaces will be termed the "small height" case, while the former set will be termed the "large height" case in what follows. The use of 64λ surface periods resulted in approximately 12800 propagating Floquet modes for the cases of interest; each processor in the parallel simulations thus considered approximately 800 Floquet modes.

The surfaces used were Gaussian random processes generated using the "Durden-Vesecky" spectrum described in [2] and [16]. This spectrum was selected because it has been applied in numerous studies of ocean-like surface thermal emission, although of course there are numerous sea spectral models that could be considered, none of which has been validated as a complete description of true sea surfaces. The spectrum parameters $a_0 = 0.008$, $d = 0.4789$, and $b_0 = a_0$ [2] were used. A fixed wind speed of $U_{19.5} = 10$ m/sec is considered in the results of Section IV; note the limitation of surface length to 64λ results in a much smaller surface rms height than a true sea surface at 10 m/sec windspeed. For this reason, investigating variations with wind speed in this simulation is not realistic. A fixed observation angle of 55 degrees (similar to many satellite radiometers) is used, along with a frequency of 19.35 GHz and a sea water relative permittivity of $29.41 + i35.98$.

The results of Section IV were obtained using supercomputing resources at the Maui High Performance Computing Center (MHPCC) [17]. A typical 64 processor run utilized 10 surface realizations; the computing time required was on the order of 2 CPU hours for each node. A total of 100 realizations were included in computing the final averages shown, with brightness results showing standard deviations typically less than 0.12 K.

IV. Results

A. Direct surface emission

Figure 1 examines direct surface emission predictions in the "small height" surface case from SSA2, SSA3, and SSA4. Variations with azimuthal angle in the four polarimetric quantities are illustrated in the four sub-plots. Results show a significant change between SSA2 and SSA3 predictions even in this small-height case, and a much smaller change from SSA3 to SSA4. Note the fourth order contribution to direct surface emission presented in [18] was incorrectly computed and underestimated; the plots shown correct this error. The SSA2 theory dramatically over-predicts the U brightness, and produces an incorrect sign in the azimuthal variation of the horizontal brightness. Average values of the linear brightnesses

also change significantly from SSA2 to SSA4. Similar trends with even larger changes are observed for the large height case in Figure 2. These results demonstrate that use of at least 2 SSA field series terms is critical for predicting surface polarimetric brightnesses; this might be expected given the fact that the second order SPM kernel (here part of $g_{\rm ssa}$) must be included in computing rough surface brightnesses in the SPM theory in order to obtain a realistic prediction. The reasonable agreement between SSA4 and SSA3 results suggests that SSA3 may be sufficient for many cases, but again the absence of the third SSA field series term in the computations makes the present SSA4 prediction incomplete. Note the current SSA4 prediction results always in a decrease in horizontal and vertical brightness temperatures from SSA3 due to the absence of the correlation term involving the third field series correction. Due to the incompleteness of the SSA4 computations, only SSA3 results are used in the following discussions.

Figures 3 and 4 compare direct surface emitted SSA3 brightnesses with predictions of the two-scale theory of [2], for the small and large height cases respectively. Two-scale model predictions (analytically averaged) were computed for continuous surfaces, but using identical parameters to the SSA simulation, including truncation of surface length scales to a maximum of 64λ. In the small height case of Figure 3, the absence of any large-scale waves makes the two-scale model identical to the passive SSA theory, and no "cutoff" wavenumber issues are involved. Good agreement between the two predictions is observed, and brightnesses are all within 0.1K. A slight underprediction of two-scale model U brightnesses by the SSA theory is observed, as well as a slight underprediction of the horizontal channel second azimuthal harmonic. The large azimuthal harmonic variations obtained by considering short scale sea waves only is directly related to the strong azimuthal asymmetry of short waves in the Durden-Vesecky spectrum.

The large height case of Figure 4 requires choice of a cutoff wavenumber k_d in evaluating two-scale model predictions. Portions of the sea spectrum below this wavenumber are classified as "large scale" and influence the long-wave slope variance only. Choices of $k_d = k_0/2$, $k_0/4$, $k_0/5$, and $k_0/10$ were evaluated: two-scale model predictions with the $k_0/4$, $k_0/5$, and $k_0/10$ choices are illustrated in the Figure. In addition results from the passive SSA theory (labeled "SPM") are included; this is essentially using the two-scale model with a k_d value of zero. Results show the choice of cutoff wavenumber to have a significant impact on two-scale model predictions in the linear polarizations, with no choice yielding a match to active SSA3 predictions for both linear channels. All cutoff wavenumber choices underpredict horizontal brightnesses, while vertical polarization is matched well only by the $k_0/5$ choice. Two-scale model predictions of U and V brightnesses are more insensitive to the cutoff wavenumber, and here significantly overpredict U results of the active SSA3 model. In order to examine the difference between maximum U brightness predictions, SSA results at 45 degrees azimuthal angle were also computed, and are included in the plots. Overall, these results make choice of an "ideal" cutoff wavenumber difficult, although the $k_0/10$ choice can be classified as uninteresting as it yields predictions very similar to the passive SSA theory. Results for the $k_0/2$ choice show even larger differences from the active SSA values.

B. Reflected atmospheric brightness

Because reflected atmospheric brightnesses were computed as both a function of azimuth angle and the zenith attenuation τ, it is most convenient to plot reflected brightness zeroth and second azimuthal harmonics versus τ. Figure 5 illustrates two-scale model predictions ($k_d = k_0/5$) of reflected zeroth azmithual harmonics for the small and large height surfaces in both linear polarizations. The large range of atmospheric brightnesses obtained as τ is varied makes plotting differences between model predictions most effective. Figures 6 and 7 illustrate SSA3 reflected atmospheric zeroth harmonics minus predictions of the two-scale model with $k_d = k_0/5$, in the small and large height cases, respectively. Differences between the two models are found to be within 0.2 K over the entire range of attenuation values for the small height case, again showing a high degree of agreement between the two theories. Differences in the large surface height case are up to approximately 2 K, with the SSA3 model under- and slightly over- predicting the two-scale theory in horizontal and vertical polarizations, respectively. Results for the two-scale theory with $k_d = k_0/4$ and the SPM model are also illustrated in Figure 7; the $k_d = k_0/4$ choice shows a sometimes similar level of disagreement to $k_0/5$ as the SSA3, although the signs of the difference are opposite for horizontal polarization. Again choice of an "ideal" two-scale model cutoff wavenumber is not possible from these results, although a disagreement of only ≈ 2 K out of atmospheric reflected brightnesses ranging up to 165K can be considered very good agreement between these theories.

SPM predictions in Figure 7 are more similar to SSA3 at low opacities, but more similar to the two-scale model in horizontal polarization at higher attenuation values. SPM reflected brightnesses were computed using equations similar to those of the SSA, but based on the first order SPM solution for non-specular bistatic scattering cross sections and the second order SPM solution for specular reflection. The degree of agreement between the SSA3 and SPM results is remarkable in the large surface height case, because, unlike the case of direct surface emission, there is no guarantee of a "small slope" behavior for reflected atmosphere computations from the SPM.

Figures 8 and 9 plot second azimuthal harmonics of the reflected brightnesses in the small and large height cases. Results from the simple approximate method based on the two-scale model ($k_d = k_0/5$) described in Section II-E for estimating atmospheric contributions to second azimuthal harmonics are also included in these Figures, and labeled "approx". Again the small height case shows an excellent agreement between SSA3 and two-scale predictions (choice of k_d is not required for this case), with differences remaining within 0.1 K. The simple approximation in Figure 8 provides reasonable predictions of U and V brightnesses, but has large

errors in the linear brightness channels. In particular, the sign of linear channel second azimuthal harmonics is incorrectly predicted by this approximation. An unusual feature in the H channel second harmonic is observed in Figure 8 when the generally decreasing trend is replaced by an increase at large τ values. A complete physical explanation of this effect is difficult at present, but it is not unreasonable given the inclusion of both atmospheric and surface scattering cross section variations with angle. Note the curves were computed at the discrete values indicated by the symbols, so that a smoother curve would result if finer sampling were used.

Results in Figure 9 for the large height case show two-scale and SSA3 predictions to be similar in most respects. Again no choice of cutoff wavenumber produces a match between two-scale and SSA3 results over all polarizations, especically for the small values of U second harmonics predicted by SSA3. Note that second harmonic contributions of the reflected atmospheric brightness are comparable at large attenuation values to those of the direct surface emission. The simple approximation again yields poor estimation of linear channel results. The opposite sign in linear polarization channels between predictions of all models and those of the simple approximation indicates that atmospheric contributions increase, rather than decrease, total brightness azimuthal variations for these channels.

V. Conclusions

The results of this study show that the active SSA, two-scale, and passive SSA models produce qualitatively similar predictions of polarimetric thermal emission and atmospheric reflection from the sea surfaces considered. The high level of agreement between the methods in the small height case serves to validate the procedure used for computing active SSA predictions. The level of error observed in the larger height case is significant, so that questions remain regarding the absolute accuracy of the three theories. Two-scale and SSA predictions showed the largest discrepancies in prediction of direct surface emitted U brightness, where the SSA predicted much smaller values, as well as the zeroth harmonic of the horizontal brightness, where the SSA predicted larger values. The large change in the predicted U brightness of direct surface emission from the SSA2 to SSA3 and SSA4 models suggests that convergence of this prediction should not be necessarily assumed. No choice of cutoff wavenumber in the two-scale model was found to produce a complete agreement with the active SSA predictions. Of course, these conclusions likely depend on the particular sea surface simulated, as well as the particular observation angle (55°) used.

Although the active SSA does not require use of a cutoff wavenumber, the overall accuracy of the theory for scattering cross sections is not established, particularly as grazing scattering angles are approached in vertical polarization. Further studies will be required to address the absolute accuracy of these theories, and as numerically exact predictions become more available progress should be possible. A related project devoted to improving the number of series terms available in the passive SSA theory [19]-[20] may also contribute to resolving accuracy questions. It should be noted that uncertainties in the sea surface spectrum, sea water permittivity, and other geophysical parameters may result in errors that dominate those from the electromagnetic model when applied to satellite data; model "tuning" based on matching satellite data will be required to develop effective spectrum and permittivity models. The basic qualitative agreement between the three electromagnetic methods indicates that such tuning based on any of the three methods should produce at least a reasonably accurate physically based forward model.

VI. Acknowledgments

This work was performed under the support of the Office of Naval Research, the Naval Research Laboratory, and the National Polar Orbiting Environmental Satellite System (NPOESS) Integrated Program Office. Use of IBM SP supercomputing resources at the Maui High Performance Computing Center is also acknowledged.

References

[1] Gaiser, P. W. et al, "The WindSAT spaceborne polarimetric microwave radiometer: sensor description and early orbit performance," *IEEE Trans. Geosc. Remote Sens.*, vol. 42, pp. 2347-2361, 2004.

[2] Yueh, S. H., "Modeling of wind direction signals in polarimetric sea surface brightness temperatures," *IEEE Trans. Geosc. Remote Sens.*, vol. 35, pp. 1400-1418, 1997.

[3] Irisov, V. G., "Small-slope expansion for thermal and reflected radiation from a rough surface," *Waves in Random Media*, vol. 7., pp. 1-10, 1997.

[4] Johnson, J. T., and M. Zhang, "Theoretical study of the small slope approximation for ocean polarimetric thermal emission," *IEEE Trans. Geosc. Remote Sens.*, vol. 37, pp. 2305–2316, 1999.

[5] Johnson, J. T. and Y. Cai, "A theoretical study of sea surface up/down wind brightness temperature differences," *IEEE Trans. Geosc. Remote Sens.*, vol. 40, pp. 66–78, 2002.

[6] Voronovich, A. G., *Wave Scattering from Rough Surfaces*, Berlin: Springer-Verlag, 1994.

[7] Voronovich, A. G., "The effect of the modulation of Bragg scattering in small-slope approximation," *Wave Random Media*, vol. 12, pp. 341–349, 2002.

[8] J. T. Johnson, R. T. Shin, J. A. Kong, L. Tsang, and K. Pak, "A numerical study of ocean polarimetric thermal emission," *IEEE Trans. Geosc. Remote Sens.*, vol. 37, no. 1 (part I), pp. 8–20, 1999.

[9] Li, S. Q., C. H. Chan, M. Y. Xia, B. Zhang, and L. Tsang, "Multilevel expansion of the sparse-matrix canonical grid method for two-dimensional random rough surfaces," *IEEE Trans. Ant. Prop.*, vol. 49, pp. 1579–1589, 2001.

[10] M. S. Gilbert and J. T. Johnson, "A study of the higher-order small slope approximation for 3-D scattering from a dielectric Gaussian rough surface," *Waves Random Media*, vol. 13, pp. 137–149, 2003.

[11] S. McDaniel, "Acoustic and radar scattering from directional seas," *Waves in Random Media*, vol. 9, no. 4, pp. 537–549, 1999.

[12] Johnson, J. T., "Third order small perturbation method for scattering from dielectric rough surfaces," *J. Opt. Soc. Am. A.*, vol. 16, pp. 2720–2726, 1999.

[13] Tsang, L., J. A. Kong, and R. T. Shin, *Theory of Microwave Remote Sensing*, Wiley, New York, 1985.

[14] Yeang, C. P., S. H. Yueh, K. H. Ding, and J. A. Kong, "Atmospheric effect on microwave polarimetric passive remote sensing of ocean surfaces," *Radio Science*, vol. 34 (2), pp. 521–537, 1999.

[15] Pierdicca, N., F. S. Marzano, L. Guerriero, and P. Pampaloni, "On the effect of atmospheric emission upon the passive microwave polarimetric response of an azimuthally anisotropic sea surface," *Progress in Electromagnetics Research (PIER) 26*, Ed. J. A. Kong, pp. 223-248, 2000.

[16] Durden, S. L. and J. F. Vesecky, "A physical radar cross-section model for a wind driven sea with swell," *IEEE J. Oceanic Eng.*, vol. OE-10, pp. 445–451, 1985.

[17] *Maui High Performance Computing Center World Wide Web Site*, on the World Wide Web at *http:www.mhpcc.edu*.

[18] Johnson, J. T., "A study of rough surface thermal emission and reflection using Voronovich's small slope approximation," *IGARSS 2004*, conf proceedings, 2004.

[19] Demir, M. A. and J. T. Johnson, "Fourth and higher order small perturbation method for scattering from a rough surface," *J. Opt. Soc. Am. A*, vol. 20, pp. 2330-2337, 2003.

[20] Demir, M. A. and J. T. Johnson, "Calculation of fourth order small slope theory of thermal emission from sea surfaces," *IGARSS 2004*, conf proceedings, 2004.

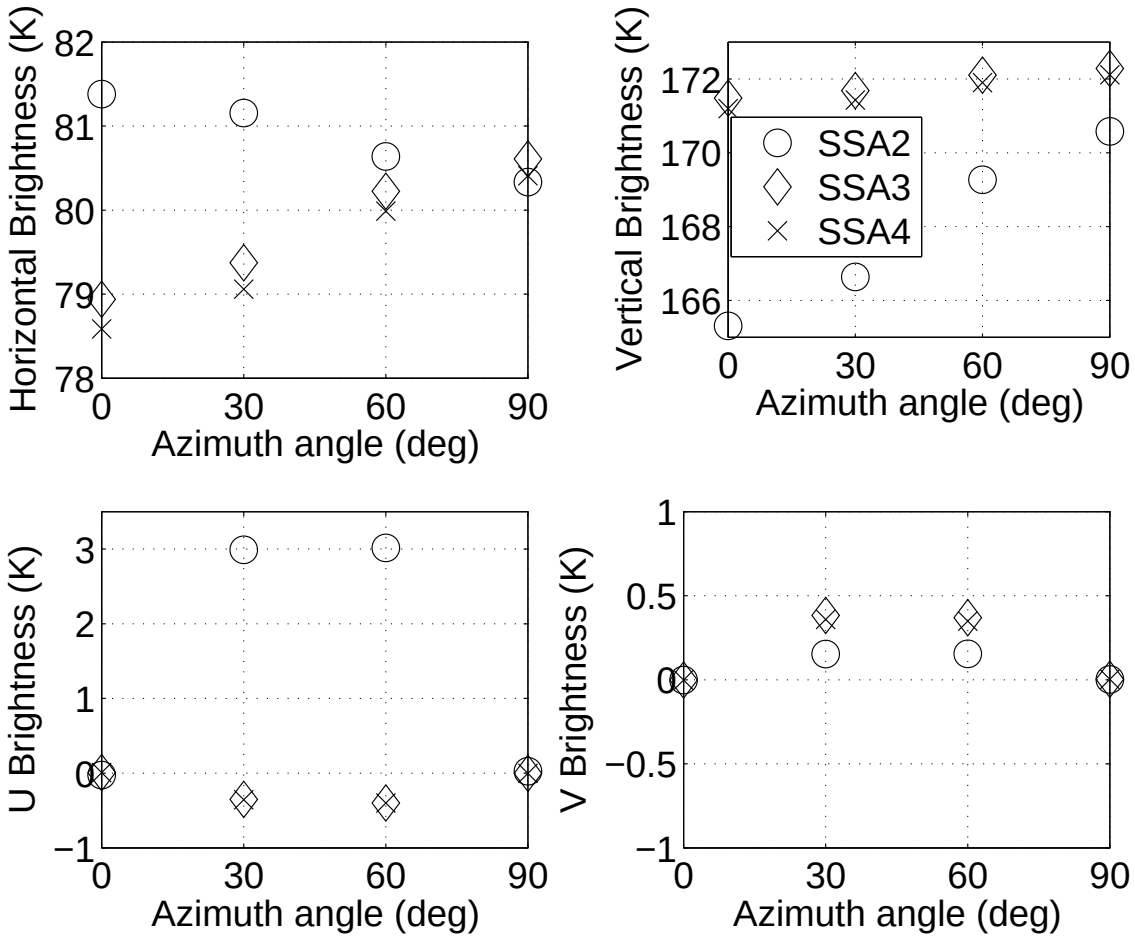

Fig. 1. Comparison of SSA2, SSA3, and SSA4 predictions for small height surface emission

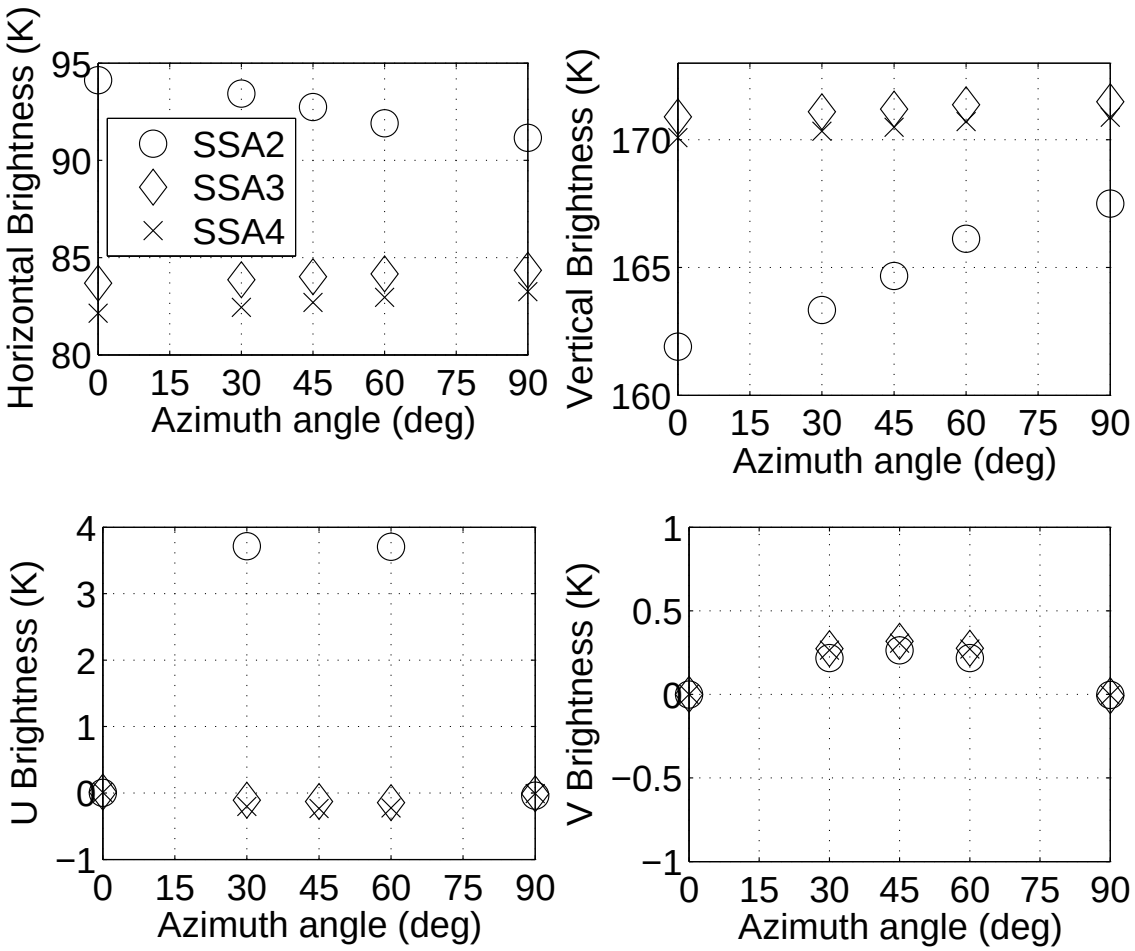

Fig. 2. Comparison of SSA2, SSA3, and SSA4 predictions for large height surface emission

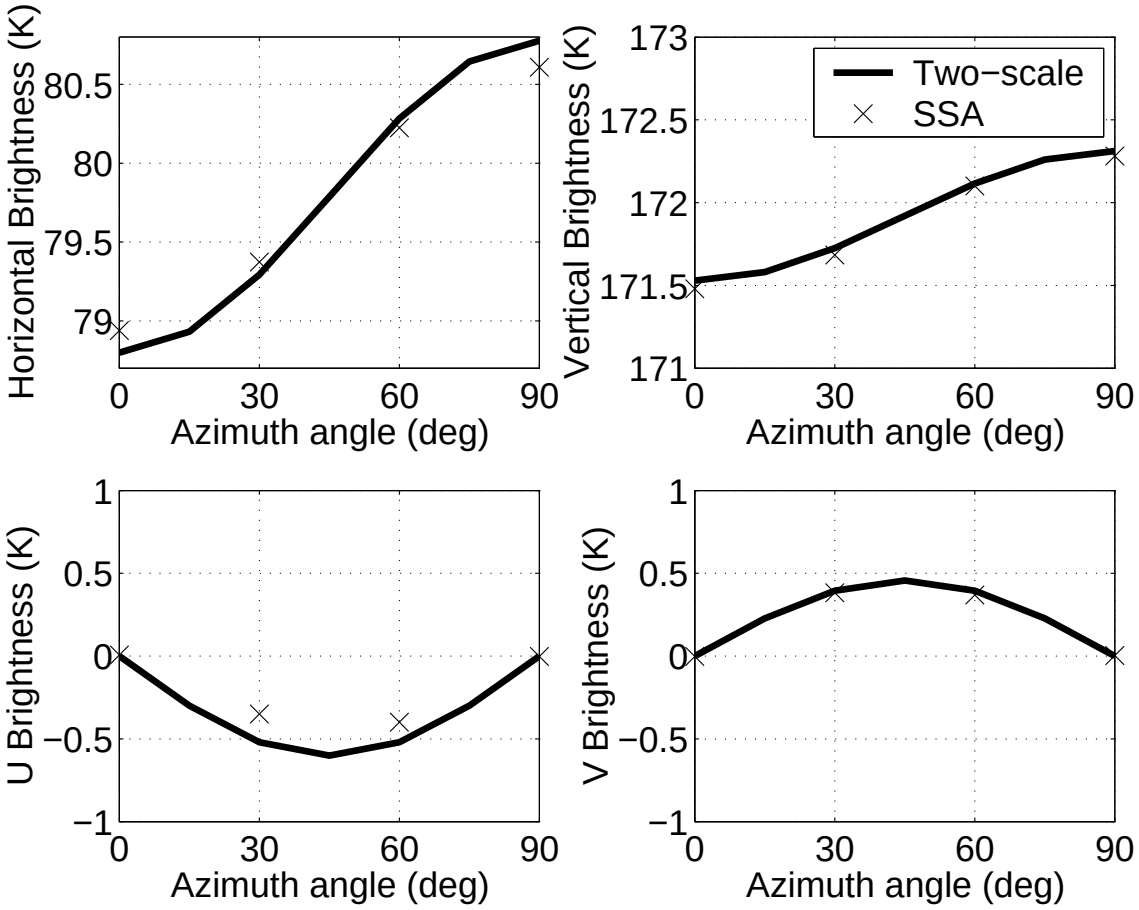

Fig. 3. Comparison of active SSA3 and two-scale predictions, small height case

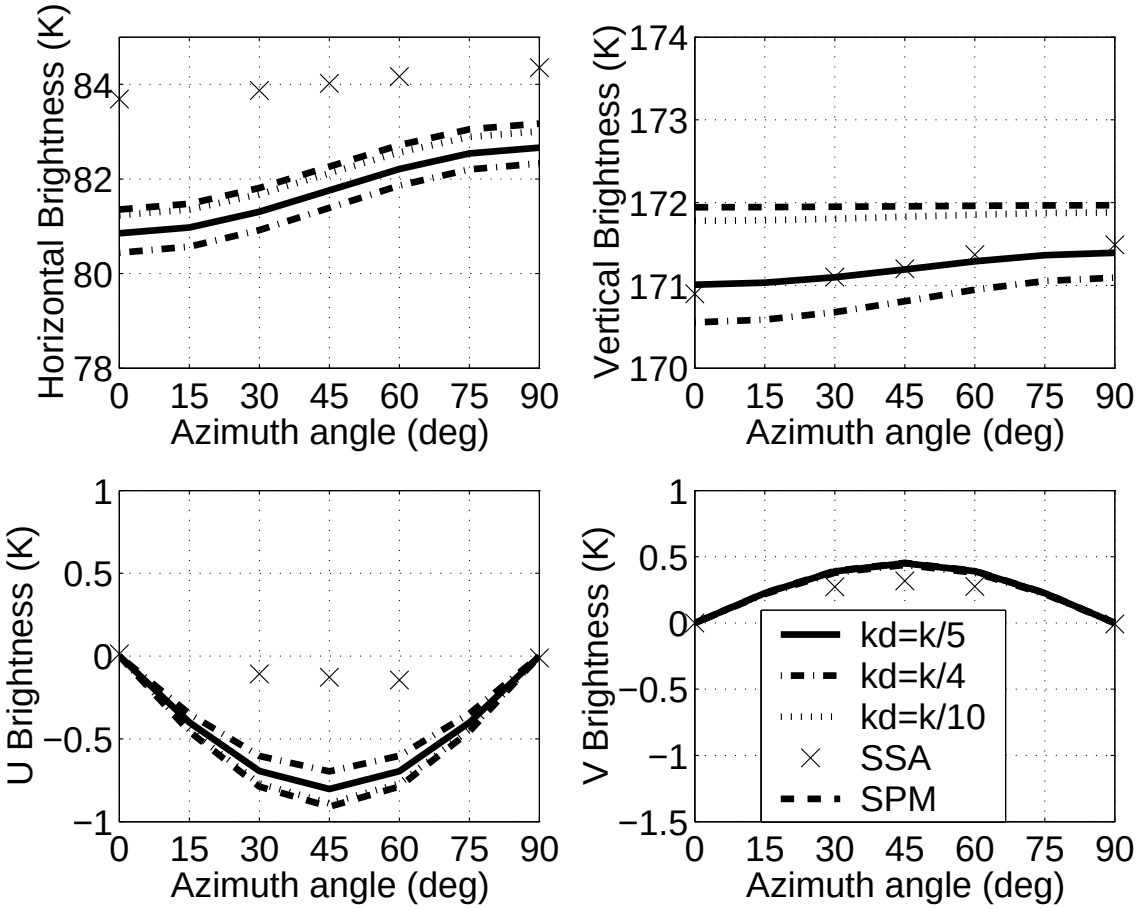

Fig. 4. Comparison of active SSA3, two-scale, and SPM model predictions, large height case

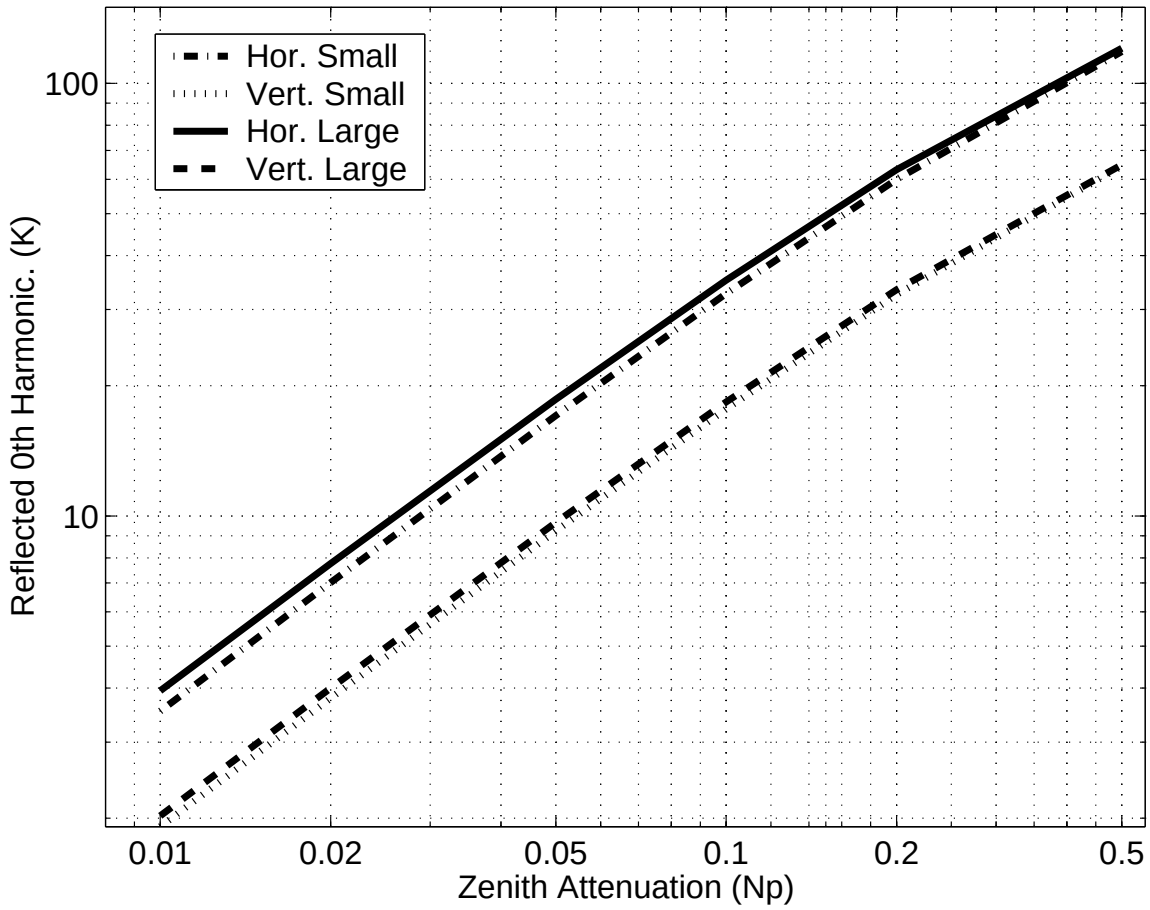

Fig. 5. Zeroth azimuthal harmonics of reflected downwelling brightness from the two-scale model ($k_d = k_0/5$)

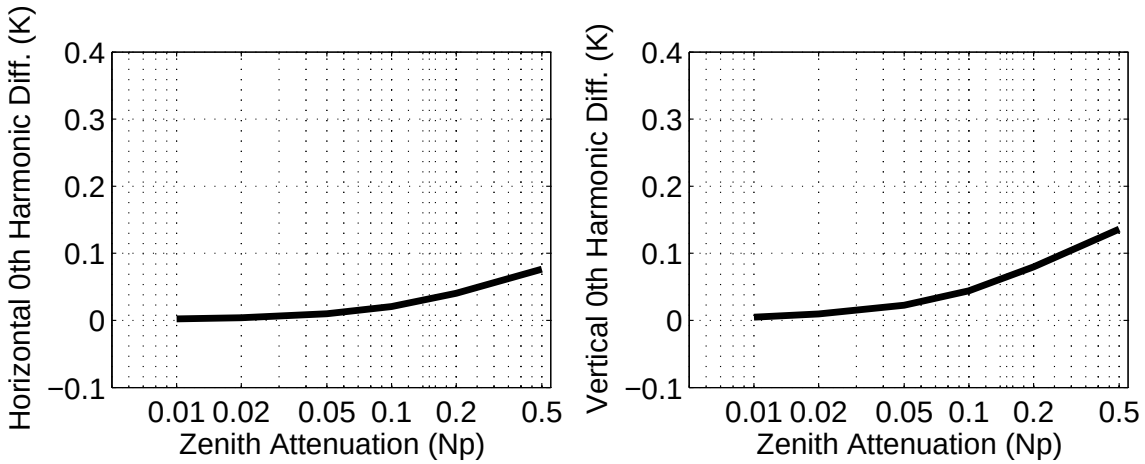

Fig. 6. SSA3 minus two-scale zeroth azimuthal harmonic of reflected downwelling brightness, small height case

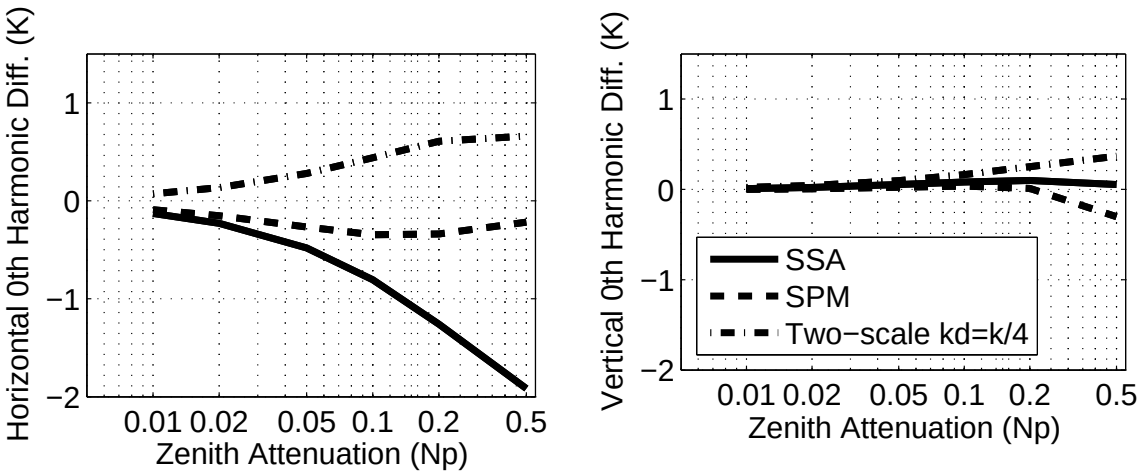

Fig. 7. Zeroth azimuthal harmonic differences of reflected downwelling brightness, large height case; two-scale model ($k_d = k_0/5$) predictions are subtracted from the models indicated

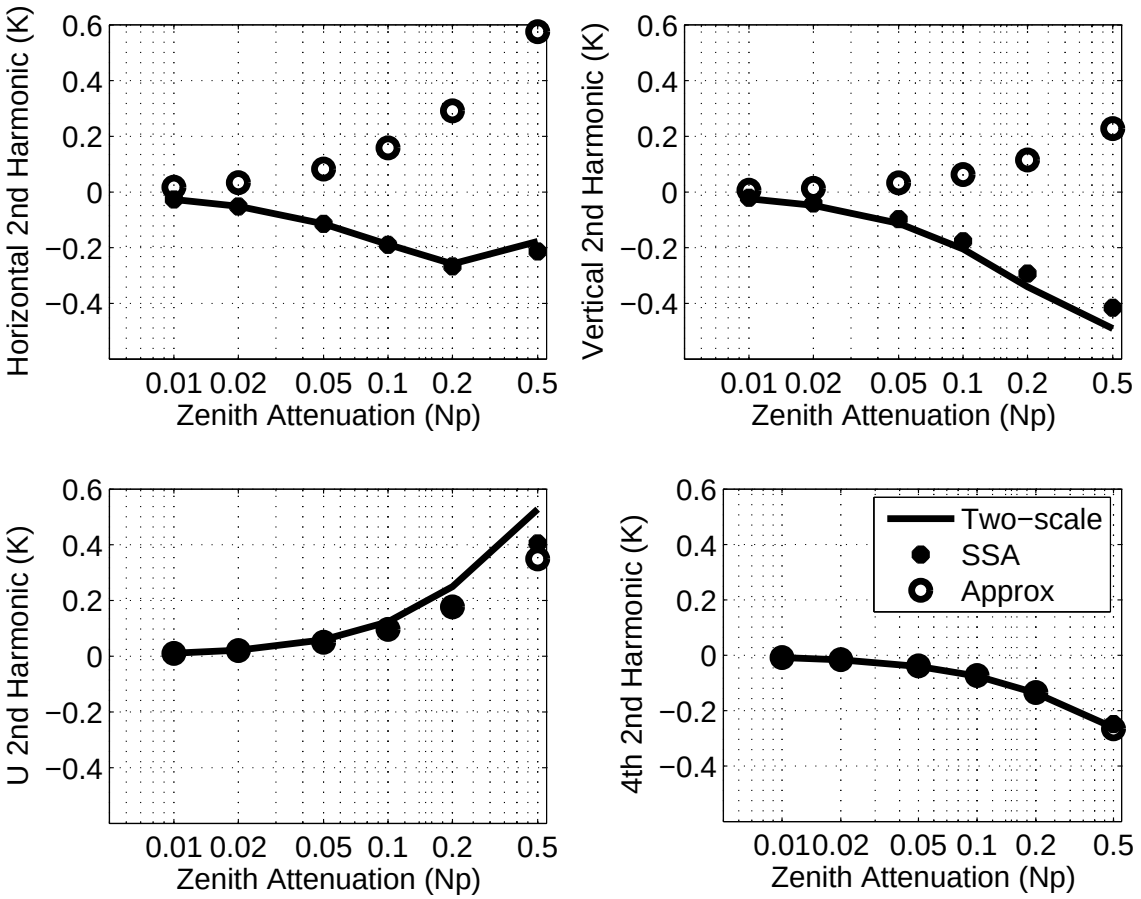

Fig. 8. Second azimuthal harmonics of reflected downwelling brightnesses from the SSA3, two-scale, and simple approximation models, small height case

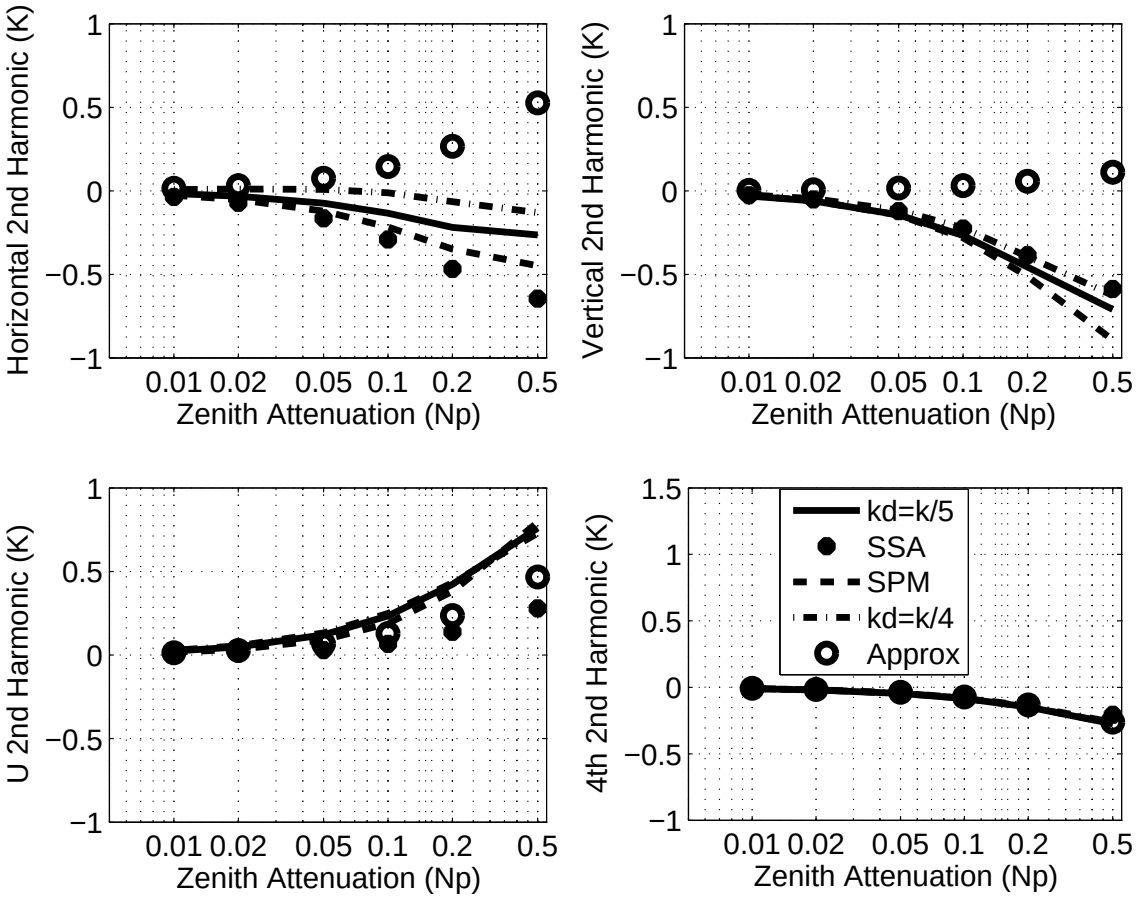

Fig. 9. Second azimuthal harmonics of reflected downwelling brightnesses from the SSA3, two-scale, and simple approximation models, large height case